Heliyon 6 (2020) e04953

Contents lists available at ScienceDirect

Heliyon

journal homepage: www.cell.com/heliyon

Research article

Synthesis, morphological analysis, antibacterial activity of iron oxide nanoparticles and the cytotoxic effect on lung cancer cell line

Subrata Das [a], Sangharaj Diyali [a], Gopal Vinothini [b], Balaji Perumalsamy [c], Gowdhami Balakrishnan [c], Thirumurugan Ramasamy [c], Dhanasekaran Dharumadurai [b], Bhaskar Biswas [a,*]

[a] Department of Chemistry, University of North Bengal, Darjeeling 734013, India
[b] Department of Microbiology, Bharathidasan University, Tiruchirappalli 620 024, India
[c] National Centre for Alternatives to Animal Experiments (NCAAE), Bharathidasan University, Tiruchirappalli 620 024, India

ARTICLE INFO

Keywords:
Inorganic chemistry
Materials chemistry
Iron oxide nanoparticles
Scanning electron microscopy images
Antibacterial activity
Cytotoxic effect
Reactive oxygen species

ABSTRACT

Focusing on the huge importance associated in developing functional materials, this research study describes the synthesis, characterization of morphology, bactericidal activity and cytotoxic effect of iron oxide nanoparticles (IONPs). IONPs have been successfully fabricated through thermal decomposition of a diiron(III) complex precursor. The morphology of the nanoparticle has been delineated with different spectroscopic and analytic methods. Scanning and transmission electron microscopy (FE-SEM and HR-TEM) analyses estimate the cross linked porous structure of IONPs with an average size ~97 nm. Dynamic light scattering (DLS) study of IONPs determines the hydrodynamic diameter as 104 nm. The cytotoxic behavior of IONPs has been examined against human lung cancer cell line (A549) through different fluorescence staining studies which ensure the mode of apoptosis for cell death of A549. Furthermore, measurement of reactive oxygen species suggests the destruction of mitochondrial membrane of *Staphylococcus aureus*, leading to effective bactericidal propensity which holds a good promise for IONPs to become a clinically approved antibacterial agent.

1. Introduction

Nano-scale functional materials hold a great promise in constructing as well as advancing nanoparticle based nano-devises than that of their bulk material [1, 2, 3]. Extensive research studies have been carried out on nano-dimensional functional materials for having their unique physico-chemical properties and their significant contributions to progress the modern science [4, 5, 6]. It is well documented that the nature of morphology of the nano-material can have great impact on the electronic characteristics, magnetic behaviours, catalytic activities, therapeutic efficacy and so on [7, 8, 9, 10, 11, 12, 13, 14, 15, 16]. Among the different kind of nano-scale materials, iron oxide nano-structures have drawn paramount attention for their employability in large scale of applications like design of nanomagnetic materials [7,8], magnetically separable nano-catalysts as well as photo-catalysts [9, 10, 11], nanomagnetic sensor [12], semiconductor and imaging devices [13], development of supercapacitors and batteries [14], improvement of coating materials [15]and others. Noteworthy, nano-scale iron oxides are found as chemically and thermally stable materials and also widely apply in applications of energy conversion [9,16].

However, in recent times, iron oxide nanoparticles grab significant attention for their use in designing therapeutics, targeted drug delivery and other biomedical applications [17, 18, 19, 20]. It is also reviewed that iron oxide nanoparticles (IONPs) are of special interest for bearing features like large surface area, small size, lower nanotoxicity, appealing magnetic properties and less hazardous in living world [21, 22, 23]. In pursuit of the importance associated with the IONPs, this research work deals with the design, synthesis, morphological analysis, bactericidal activity and antiproliferative effect of iron oxide nanoparticles. Thermal decomposition technique was employed to produce IONPs. SEM and TEM images, PXRD and other spectroscopic methods were used to depict the morphology of the nanoparticles. DLS study was employed to estimate the hydrodynamic size of IONPs. ROS measurement and loss of trans-membrane potential study against *S. aureus* bacterial species as well as mitochondrial depolarization pattern observation ensures about the potentiality of IONPs to become a promising candidate for clinically

* Corresponding author.
E-mail addresses: bhaskarbiswas@nbu.ac.in, icbbiswas@gmail.com (B. Biswas).

https://doi.org/10.1016/j.heliyon.2020.e04953
Received 5 June 2020; Received in revised form 13 July 2020; Accepted 11 September 2020

approved antibacterial agent. The cytotoxic behaviour has been evaluated towards human lung cancer cell line (A549) through different fluorescence staining methods.

2. Experimental

2.1. Preparation of the precursor

2.1.1. Chemicals, solvents and starting materials

High purity salicyaldehyde (Sisco Research Laboratories Pvt Ltd, India), 1,3-diaminopropan-2-ol (Sigma-Aldrich, UK) and iron(III) chloride hexahydrate (Merck, India) were purchased from the respective sources. All the chemicals including solvents were of Analytical grade (A.R. grade) and used as received.

2.1.2. General synthesis of the Schiff base (H_3**L**), its diiron(III) compound and iron oxide nanoparticles

The compartmental Schiff base, H_3**L** and its diiron(III) complex were prepared following a reported synthetic route [24, 25, 26, 27, 28]. The Schiff base was synthesized by condensing salisaldehyde (2 mmol, 0.244 g) and 1,3-diaminopropan-2-ol (1 mmol, 0.086 g) in 25 mL ethanol under reflux for ~10h. Thereafter, the reaction mixture was evaporated to yield a yellow crystalline product. The Schiff base was stored over $CaCl_2$. Yield, 0.272 g (82.4%). Anal cal. for $C_{17}H_{18}N_2O_3$ (H_3**L**): C, 68.48; H, 6.08; N, 9.39; Found: C, 68.40; H, 6.02; N, 9.35. IR (KBr, cm^{-1}): 1630 (s), 3375 (s), UV-Vis (λ_{max}, nm): ~221, 256, 316, 403.

The diiron(III) complex was synthesized by dropwise addition of aq. methanolic solution (5 mL) of $FeCl_3.6H_2O$ (0.540 g, 2 mmol) into a 10 mL methanolic solution of H_3**L** (0.298 g, 1 mmol) with slow stirring. Then solid sodium furoate (0.134 g, 1 mmol) was added in small portions into the red coloured reaction mixture and stirring was extended to 10 min more. The reddish brown reaction mixture was kept in open air and after 7–9 days, suitable single crystals of diiron(III) complex were separated out. The brown coloured crystalline product was dried over silica gel. Yield: (on metal salt basis) 0.399 g (74.0%). *Anal. cal.* for $C_{23}H_{24}N_2Cl_2O_8Fe_2$ (**1**): C, 43.36; H, 3.79 N, 4.39; Found: C, 43.31; H, 3.75; N, 4.36. Selected IR frequencies (KBr pellet, cm^{-1}): 3485 (s), 1621 (s), 1507 (s), 1428(s), 1378(m), 802(m). UV-Vis (λ, nm, 10^{-4}, MeOH): 234, 322, 502.

The IONPs were produced following the thermal cleavage of this diiron(III) complex as a precursor. Previously, we had reported the X-ray structure of the diiron(III) complex. The crystal structure exhibited the existence of an alkoxido-acetato-bridged diiron(III) compound in crystalline phase where each of the iron(III) centres adopt octahedral coordination geometry. The thermal decomposition profile (Figure 1) of the diiron(III)-Schiff base complex showed stepwise decomposition of the metal complex. The precursor produced thermally stable iron oxide nanoparticles (IONPs) (expt. wt loss = ~80% at 685 °C) upon heating at 700 °C for 3h in a furnace. This is also evident from the comparison of IR spectra between a standard iron oxide and the end product of thermal decomposition for diiron(III)-precursor. Other spectroscopic results of the end product agree very well with the existence of IONPs in the form of Fe_2O_3 (Figure 2).

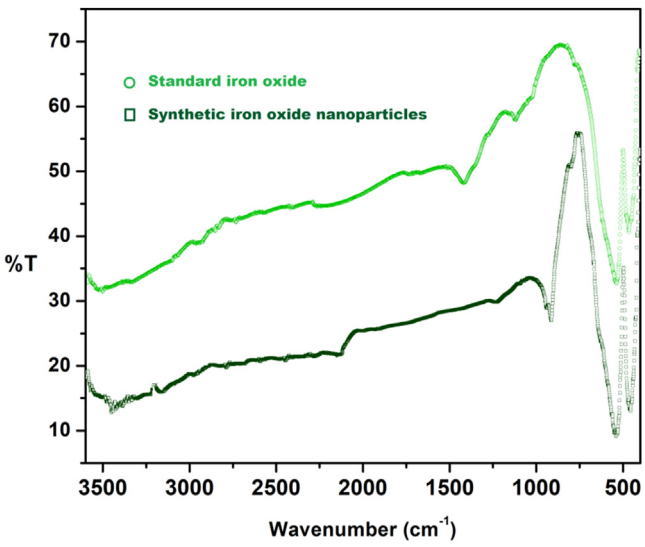

Figure 2. IR spectra of IONPs and standard iron oxide.

2.2. Physical measurements

A spectrophotometer (FTIR-8400S SHIMADZU) was employed to record infrared spectrum (KBr) of diiron(III) complex and IONPs in the range 400–3600 cm^{-1}. NMR spectra were recorded with a Bruker Avance 300 MHz spectrometer in DMSO-d_6 at 25 °C. The absorption spectra were measured with a JASCO V-730 UV-vis spectrophotometer. Thermal analysis was performed with a Perkin Elmer Diamond TG/DTA system in a static nitrogen atmosphere with a heating rate of 10 °C/min. Elemental analyses were carried out in a Perkin Elmer 2400 CHN microanalyser.

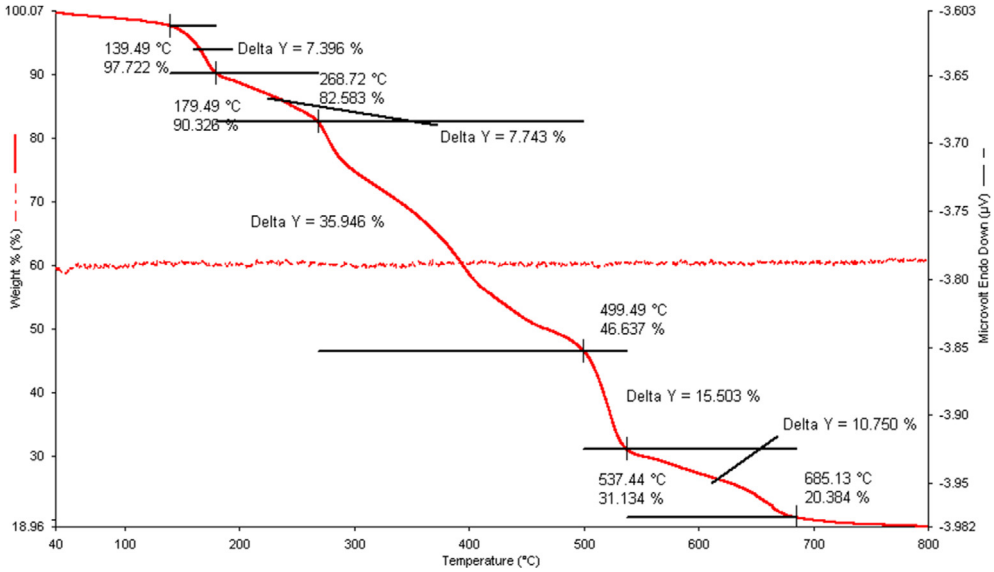

Figure 1. Thermogravimmetric analysis spectrum of the diiron(III) complex.

The dynamic light scattering study and zeta potential measurement of the IONPs were performed at 25 °C on a Malvern Instrument with Zetasizer Nano ZS90 instrument. The hydrodynamic size of IONPs was measured by adding 100 μL of IONPs solution to 1.5 mL of water and recorded in triplicate to find an average number-size distribution.

2.3. Physicochemical characterization of iron oxide nanopartcles

The morphology of the iron oxide nanoparticles (IONPs) was determined by X-ray diffractometer (Bruker D8 advance) using CuK_{α} radiation ranging from 20°-80°. The size and shape of the IONPs were assessed through scanning electron microscopy (FE-SEM, HR-TEM) images. The SEM images were recorded using a microscope in JSM-6700F FESEM, JEOL, Japan and TEM images were obtained on a JEM-2100 HRTEM, JEOL, Japan.

2.4. Antibacterial activity of iron oxide nanopartcles

The *in vitro* bactericidal study of the IONPs was performed against different pathogenic bacteria like *Staphylococcus aureus, Proteus vulgaris* and *Pseudomonas aeruginosa* following the method of well diffusion [29]. The pathogenic bacteria were cultured in nutrient broth followed by incubation for 24 h at 37 °C. Afterwards, 100μL (10^6 CFU/mL) of the respective indicator strain was added to the nutrient agar plates to prepare the turf of bacterial culture. 100 μL of the IONPs with a concentration of 1 mg/mL was loaded to the wells which were developed by boring the agar with a sterile borer. All the plates were incubated for 37 °C for 24 h and subsequently, the zone of inhibition diameter (mm) for each compound were recorded to compare with the inhibition diameter of antibiotic streptomycin.

2.4.1. Minimum inhibitory concentration by resazurin assay

2.4.1.1. Preparation of resazurin. The resazurin solution was prepared by the addition of 0.015 g resazurin to 100 mL sterile distilled water. The solution was vortexed and sterilized (0.22 μM filter), and kept in a brown bottle.

2.4.1.2. Resazurin microtitre assay (RMA). The minimum inhibitory concentration (MICs) of IONPs was detected with RMA following the method described by Norazah *et al.* (2017) [30]. 100 μL of IONPs with a concentration of 2 mg/mL was added into the first row of the 96-well micro titre plate. The remaining wells were filled with 50 μL of nutrient broth. Each well with 50 μL of the test compound having descending concentrations in a serial manner were performed by two fold serial dilutions. Finally, 10 μL of *Staphylococcus aureus* was added to the well to attain a final concentration of 5×10^6 CFU/mL. This experiment had two set of controls: a negative control indicates column with normal saline and a positive control represents a column with antibiotic (streptomycin). After incubation for 24 h, the titre plates were stained by addition of 10 μL of resazurin (0.015 %) and kept in re-incubation for another 2–4 h at 37 °C to observe the colour change. The change in colour from blue to pink revealed that the reduction of resazurin to resorufin occurred and ensured the presence of bacterial growth. The MIC expressed the minimum concentration of IONPs which didn't exhibit the change of colour.

2.4.1.3. Oxidative stress study. The development of reactive oxygen species (ROS) was assessed employing 2′,7′-dichlorodihydrofluorescein diacetate (DCFH-DA) as a peroxynitrite indicator which is capable to distinguish both nitric oxide and hydrogen peroxide inside and outside of the cells [31,32]. 100 μL suspension of *Staphylococcus aureus* (5×10^6 CFU/mL) was treated with 200 μM DCFH-DA, and fluorescence emission was measured at 505 nm with a Synergy H1 hybrid reader (Biotek, USA) with an excitation at 480 nm. 100 μL IONPs at MIC concentration was added to the above mixture at log phase of the growth kinetics. The variation of ROS was estimated by comparing the fluorescence intensities with that of the control (non-treated IONPs suspensions). The experiments were performed in triplicate.

2.5. Protocol for biological activities

2.5.1. Cell culture

Human lung cancer cell line, A549 was procured from the National Center for Cell Science (NCCS), Pune, India followed by cultured in DMEM high glucose medium (Sigma-Aldrich, USA), consisting of 10% fetal bovine serum and 2% of penicillin/streptomycin (Gibco, Thermo Scientific, USA). The cell culture was incubated in a CO_2 incubator with humidified atmosphere at 37 °C temperature and 5% CO_2 (Thermo Scientific, USA). For experiments, the cell passage 15 or less was used.

2.5.2. Cell viability assay

The percentage of cell viability inhibited by IONPs was measured adopting 3-(4,5-dimethylthiazol-2-yl)-2,5-diphenyltetrazolium bromide (MTT) assay [33]. The stock solution of IONPs in dimethyl sulfoxide (DMSO) was diluted with the culture media to obtain the working solution of different concentrations. The 96 well plate seeded with 5×10^3 A549 cells per well was treated with working solution and incubation for 24 h. DMSO solution has been used as solvent control. At each well after incubation, 20 μL of MTT solution (5 mg/mL in PBS) was added and the plate was covered by aluminum foil and incubated at 37 °C for 4h. After which 100 μL of DMSO was added to every well for the dissolution of formazan crystals. The absorbance was monitored at 570 nm using microplate absorbance reader (iMark™, Bio-Rad, USA). The mean average was derived from three separate experiments integrated into the following formula to measure the inhibition percentage:

$$\frac{\text{Mean of absorbance of untreated cells (Control)} - \text{Mean of absorbance of treated cells}}{\text{Mean of absorbance of untreated cells (Control)}} \times 100$$

2.5.3. Acridine orange (AO), ethidium bromide (EB) and hoechst 33258 staining studies

The IONPs mediated apoptosis cell death was assessed using fluorescent based AO/EB and Hoechst 33258 staining methods [34,35]. The procedure involves treating cells with IC_{50} concentration of IONPs derived from MTT assay, harvesting cells to prepare cell suspension, and staining of 5×10^5 cells/mL with 25 μL of fluorescent dyes. The untreated cells serve as controls. The working solution of AO/EB was prepared by mixing 3.8 μM of AO and 2.5 μM of EB, while 33258 dye was prepared as 1 mg/mL of hoechst. The stained cells were examined under fluorescent microscope (Carl Zeiss, Axioscope2plus) with UV filter of 450–490 nm for AO/EB and 355–377 nm for hoechst 33258.

2.5.4. Assessment of mitochondrial membrane potential (ΔΨm) (JC1 staining)

The mitochondrial trans-membrane potential of IONPs treated and non-treated/control cells were evaluated using JC1 staining method [36]. The staining involved cultivating cells on glass cover slips (22/22 mm) and exposed them with IC_{50} concentration of IONPs. The cells were stained with JC-1 dye after an incubation of 12 h. The untreated cells were grown as control. After staining the fluorescence emission was observed at ~590 nm in the fluorescent microscope to evaluate the ΔΨm.

3. Results and discussion

3.1. Synthesis of the iron oxide nanoparticle (IONPs)

The iron oxide nanoparticle (IONPs) were synthesized by thermal decomposition of the diiron(III)-Schiff base precursor at 700 °C for 3h in a furnace. The diiron(III) complex was thermally cleaved in a stepwise manner under N_2 atmosphere to produce iron oxide nanoparticles (Figure 1). The diiron(III) precursor yields iron oxide nanoparticle in high efficiency as a thermally stable product. The decomposition profile for the diiron(III)-Schiff base precursor is previously reported [24]. The composition of iron oxide nanoparticle was determined through different spectroscopic methods as well as powder X-ray diffraction studies. The schematic presentation of the synthetic route of iron oxide nanoparticle using thermal decomposition technique is given in Scheme 1 and presented below.

3.2. Physico-chemical characterization of IONPs

Different spectroscopic methods have been employed to characterize the iron oxide nanoparticles (IONPs). Infrared spectrum of the thermally decomposed end product displayed characteristics peak at 511 cm^{-1} which is attributed to M-O (Fe–O) stretching of the IONPs and shown in Figure 2 [25]. No other characteristic peaks have been found in IR spectrum of IONPs and ensures about the high purity of synthetic IONPs. The formation of IONPs is further authenticated as evident from the comparison of IR spectra for a standard iron oxide and IONPs.

PXRD studies have been carried out to find the morphology as well as crystalline features of IONPs. All the diffraction peaks of IONPs (Figure 3) are well indexed with the diffraction pattern of standard iron oxide nanoparticles. CELSIZ programme was employed to obtain the lattice parameters of IONPs as $a = b = c = 8.3512$ (3) Å. PXRD study also reveals that IONPs exist in cubic structure with $P4_132$ space group (Figure 3). No other diffraction peaks corresponding to impurity are observed which authenticate the high purity of the synthetic IONPs. The diffraction pattern of IONPs is well indexed with the diffraction pattern of Fe_2O_3 compound. Scherrer's equation [37] has been applied to determine the average crystallite size of IONPs using PXRD data as follows (Figure 4):

$$L = \frac{k_s \lambda}{(cos\theta)\tau}$$

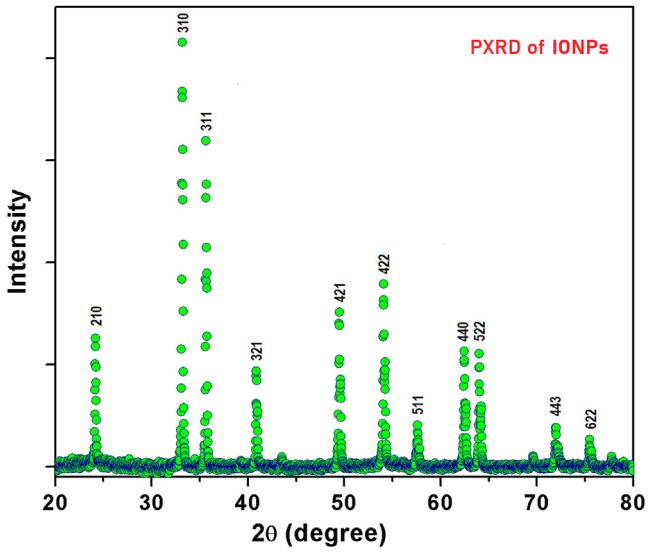

Figure 3. PXRD plot of IONPs.

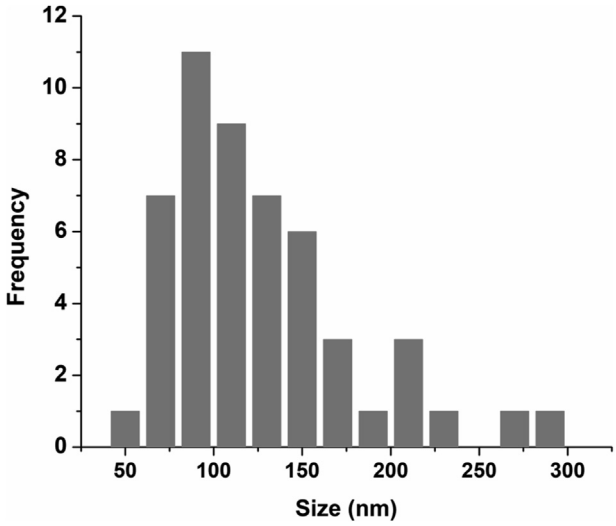

Figure 4. Size distribution plot of IONPs derived from Scherrer's equation using PXRD data.

Where L is average crystallite size, k_s is the proportionality coefficient = 0.9, λ indicates the X-ray wavelength = 1.5406Å, τ is the peak width at full width at half maxima in radians, and θ is the Bragg's angle. The histogram of particle distribution of IONPs obtained from PXRD is given in Figure 4. The average crystallite size is determined as 97 (±3) nm.

The hydrodynamic diameter was also measured by dynamic light scattering (DLS) study. Figure 5 represents the DLS profile of IONPS. The

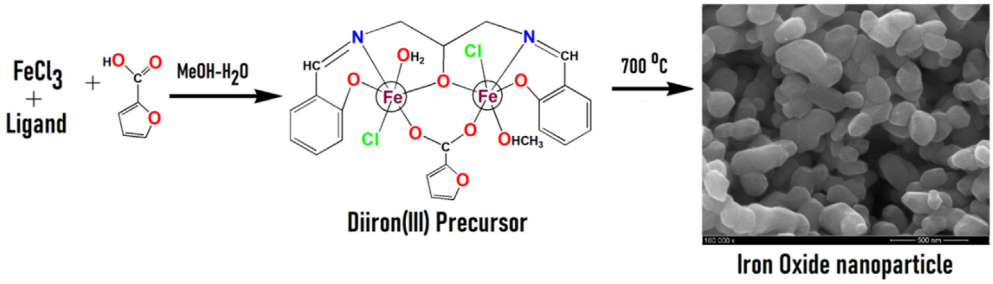

Scheme 1. Preparative procedure of the diiron(III) precursor and IONPs.

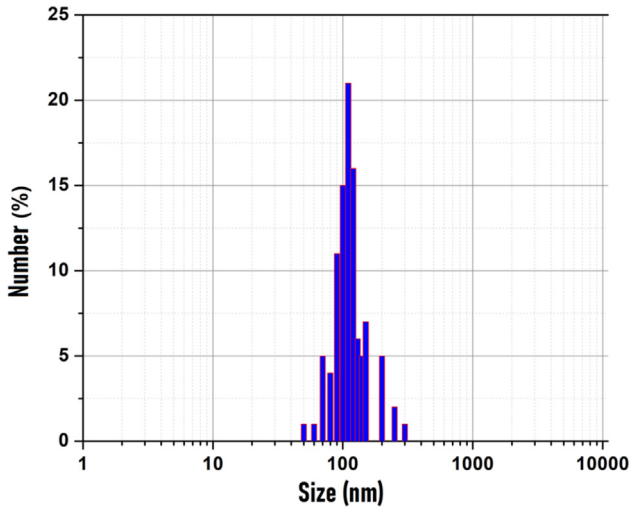

Figure 5. IONPs size distribution as measured by dynamic light scattering.

hydrodynamic size measurement suggested that IONPs had an average size of 104 nm. The average zeta potential of IONPs was calculated as -12.1 mV in DMSO dispersant. This low value probably ensures the steric repulsion among IONPs in DMSO. This may be attributed to the hydrophilic nature of the IONPs which prevents agglomeration. Similar observation was reported by Tran *et al.* during his study of antibacterial activity of iron oxide nanoparticle on *Staphylococcus aureus* [38].

An electronic spectrum of IONPs has been measured in DMSO medium ranging from 200 nm to 700 nm (Figure 6). An electronic band with high absorbance and one broad optical band were observed at 265 and 369 nm respectively for the IONPs. The characteristic band at 265 nm is attributed to n→σ* electronic transition while the electronic band appeared at 369 nm is assignable for n→π* electronic transition for the synthetic IONPs [25]. It is commonly observed that the particle size of IONPs depends on concentration of DMSO. Previously reported data further supports this observation [39]. In order to justify the stability of IONPs in DMSO, we recorded electronic spectra of IONPs solution at different time interval (1^{st}, 3^{rd}, 5^{th} days). The position of electronic bands for IONPs in this time frame remains almost unaffected (Figure 6). The electronic bands for IONPs are well documented in reported literatures [9,18]. Thus, IONPs were stable in DMSO for five days.

The energy of band gap for the IONPs was determined based on the appearance of the electronic bands in the absorption spectrum of IONPs

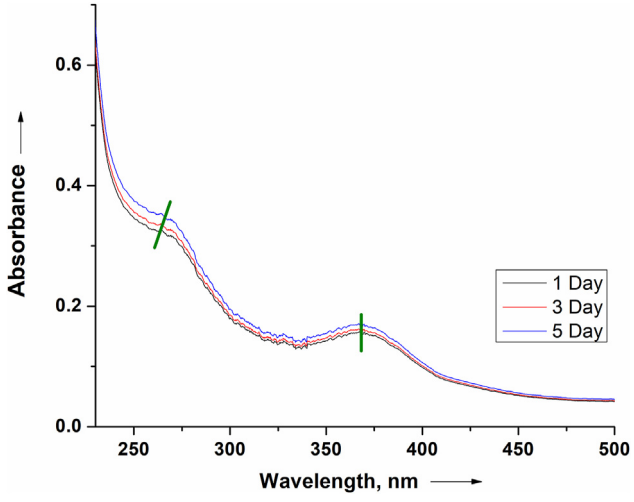

Figure 6. Electronic spectra of IONPs recorded on 1st, 3rd and 5th day in DMSO.

following the equation, $E_{bg} = 1240/\lambda$ (eV), where, E_{bg} presents the energy of band gap for the photocatalyst and λ indicates wavelength in nm. The band gap energy of IONPs is calculated as 3.36 eV (Figure 6). This band gap energy of IONPs is suitable to act as a good photo-catalyst. The spectroscopic and morphological characterization of these IONPs along with synthetic method was partially reported elsewhere [40].

3.3. Scanning electron microscopy analysis

FE-SEM and HR-TEM were employed to examine the surface morphology, size and shape of IONPs. In the light of micrographs of SEM (Figure 7), it is revealed that a mixture of hexagonal and elliptical shaped nanoparticles co-exists together with an average individual size of the nanoparticle is ~97 nm. However, the distribution of elliptical shaped particles is dominant in the mixture. Most of the individual nanoparticles vary from 50 to 120 nm in size for these synthetic IONPs. Figure 7 presents the image of pure IONPs portrayed that individual grain size of IONPs is ~97 nm.

HR-TEM images (Figure 8) are also recorded for better understanding of surface morphology and size of the IONPs. HR-TEM analysis displayed similar kind of surface morphology as evident from FE-SEM. Close look at surface morphology of IONPs ensures that individual nanoparticles have well defined surface barrier ranging from 50 to 100 nm size and elliptical shape. Therefore, scanning electron microscopy image analyses are in well agreement about the particle size distribution and shape of the individual nanoparticles of IONPs.

3.4. In vitro antibacterial activity

The bactericidal activity of IONPs was studied against different pathogenic bacteria employing well diffusion method. The tested IONPs exhibited notable bactericidal activity through developing large inhibition zone. The IONPs exhibited a good inhibitory activity against different pathogens (Figure 9). It was observed that the IONPs displayed a little bit lesser activity compared to that of the standard drug, streptomycin. The bacteria, *Staphylococcus aureus* was justifiably chosen for further MIC assays. The efficiency of destruction of IONPs against different bacteria depends on important factors including physico-chemical properties, concentration, nature of bacterial species, impermeability of the cell wall and differences in ribosome of microbial cells [41].

3.4.1. Minimum inhibitory concentration by RMA

The non-toxic resazurin is a blue non-fluorescent dye which is widely employed to evaluate the cell growth. The metabolically active cell in bacteria induces irreversible reduction of the blue dye, resazurin to turn on a highly fluorescent pink, resorufin which is subsequently reduced to a colourless and non-fluorescent molecule, hydroresorufin by oxidoreductase within viable cells. Such colour change can be observed visually and thereby spectrophotometer isn't employed in this microtitre on resazurin was adopted to reveal the effect of inhibition of IONPs against *S. aureus*. The MIC of the IONPs was determined as 12.5 μg ml^{-1} against *S. aureus* (Figure 10). Actually, antibacterial study of five samples including these IONPs was concurrently carried out. Column 4 and column 5 represents the negative control (containing phosphate buffered saline, growth medium and bacteria) and the positive control (containing streptomycin, growth medium and bacteria) respectively.

3.4.2. Mechanistic insights of antibacterial activity of IONPs

Scientific experiments proves that development of hydroxyl radicals, superoxide radicals, singlet oxygen, and hydrogen peroxide as summarized as reactive oxygen species (ROS) may cause the damage in proteins as well as DNA of the bacteria and leading to bactericidal activity in IONPs through oxidative stress [42, 43, 44]. Nevertheless, the generation of free radicals in the oxido-reduction process remains the driving force to introduce oxidative stress on the bacterial cells and transform them

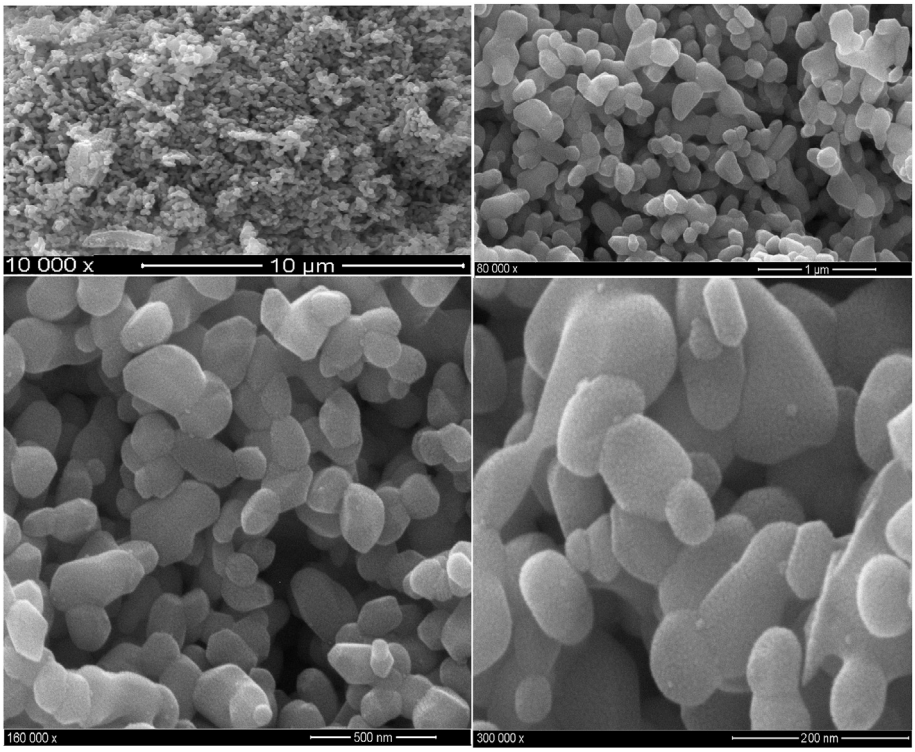

Figure 7. FE-SEM micrographs of IONPs at different magnification.

non-viable (Scheme 2). Stronger the interaction, stronger will be development of ROS which caused the destruction of the bacterial membranes [45]. Usually, antimicrobial agents able to release active ionic species through interaction between active sites (–SH) of the proteins in bacterial cell with antimicrobial agents and introduce cell lysis [42].

In general, nano-scale material may effectively interact with intracellular oxygen and may put oxidative stress on cell membrane which can trigger the interference of the cell membrane. The Antibacterial effect of the IONPs on three different bacterial species is summarized in Figures 9 and 11. The zeta potential for IONPs was found as -12.1 mV in DMSO

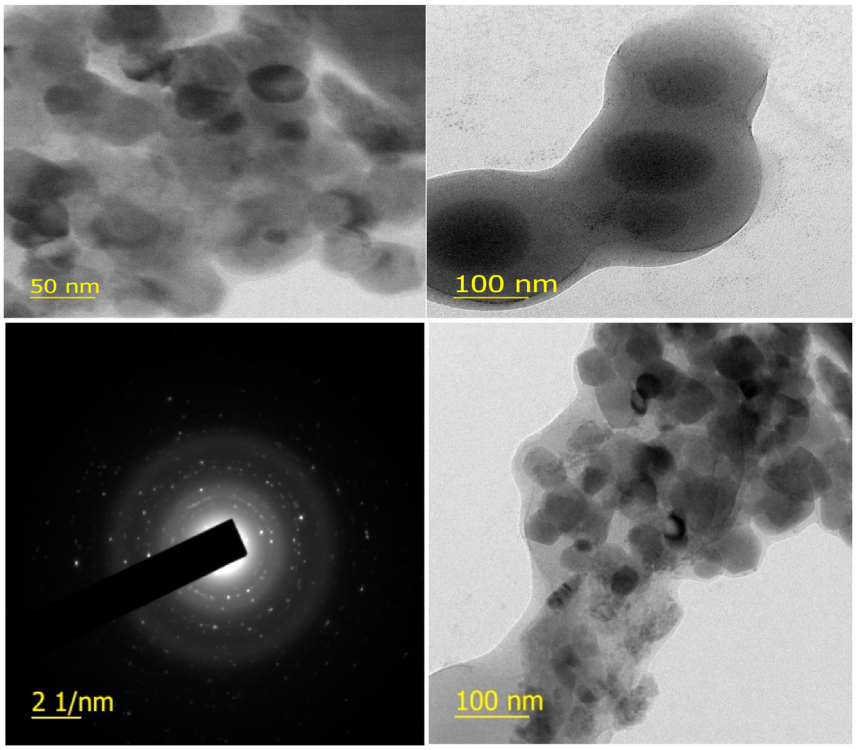

Figure 8. HR-TEM images of IONPs at different magnification.

dispersant at 25 °C. The IONPs exhibited greater sensitivity towards gram-positive bacteria (*S. aureus*) and displayed lower activity towards gram-negative bacteria (*P. vulgaris, P. aeruginosa*). In this case, the greater bactericidal activity can be manifested on the electromagnetic interaction between oppositely charged IONPs and *S. aureus* leading to the development of ROS which subsequently put an oxidative stress through oxido-reduction processes.

In order to confirm the bactericidal property of IONPs, ROS measurement studies of *S. aureus* in presence of IONPs at MIC concentration was performed. Figure 11 shows the kinetics for the DCFH-DA oxidation of bacterial cell upon treatment with IONPs. IONPs were added in log phase of bacterial growth. ROS was also traced in absence of IONPs. Scientific documents prove that ROS can also develop under non-stress conditions and may counteract by ROS scavenging enzymes in *S. aureus* bacteria such as superoxide dismutase (SOD). Nevertheless, IONPs (Figure 11) enhance the fluorescence intensity significantly which is directly correlated with the quantity of ROS developed for *S. aureus* bacterial cells. The increment nature of ROS in *S. aureus* upon treatment of IONPs bacterial cell may cause the damage of iron-sulphur clusters as well as IONPs and thereby release ferrous ion. Now, these Fe^{2+} ions can react with H_2O_2 to produce hydroxyl radical through Fenton reaction and can destroy DNA, lipid and proteins of the bacteria [46]. This phenomenon manifests the bactericidal activity in IONPs through oxidative stress which blocks the synthesis of proteins and causes a restriction to further growth of the organism. This is further evident from the depolarization effect in JC-1 staining (Figure 13). The bactericidal efficiency of IONPs increased with increase in concentration and acts as a dose dependent drug. Therefore, the growth inhibition of the bacterial species is the reflection of cell destruction induced by nanomaterials [41, 42, 43, 44, 45, 46, 47, 48, 49]. Previously, Arakha *et al.* and Lee *et al.* showed similar kind of antibacterial effect induced by IONPs [42,49].

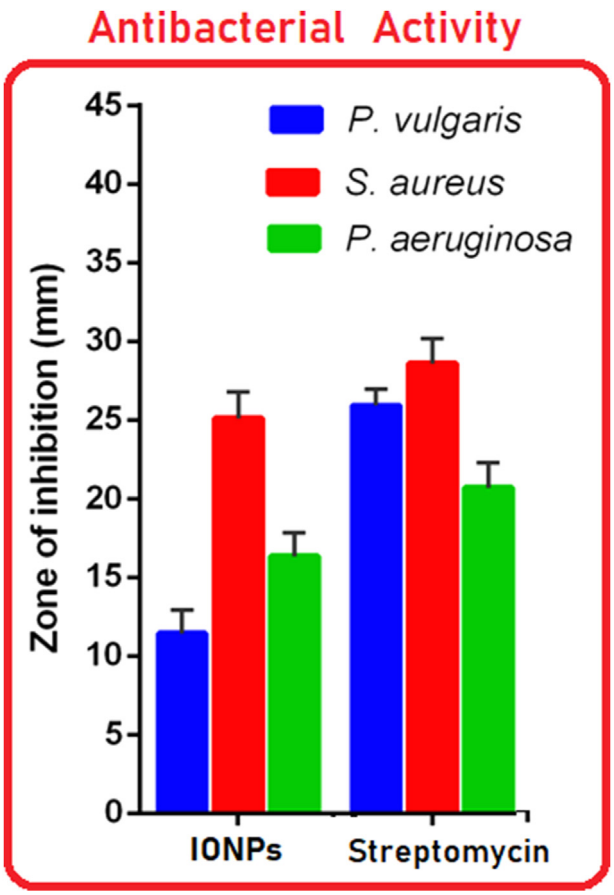

Figure 9. Inhibitory effects of the IONPs and streptomycin against pathogenic bacteria using well diffusion assay. The results were compared with the control.

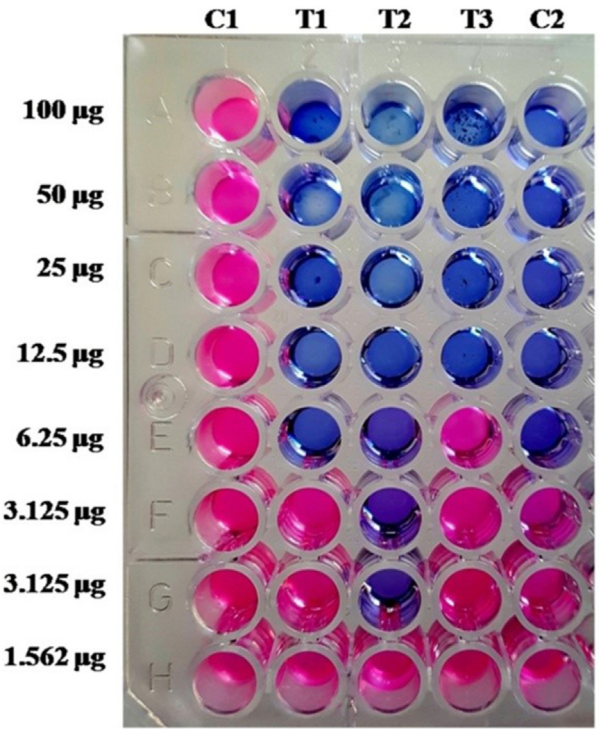

Figure 10. Minimum inhibitory concentration of IONPs with various compounds against *S. aureus* using RMA. C1- Negative control [Broth + phosphate buffered saline (2 fold diluted) + bacteria + dye]; T1- [Broth + Au(III)-bipy complex **1** (2 fold diluted) + bacteria + dye]; T2- [Broth + Au(III)-phen complex **2** (2 fold diluted) + bacteria + dye]; T3 [Broth + iron oxide nano (2 fold diluted) + bacteria + dye]; C2- Positive control [Broth + Streptomycin (2 fold diluted) + bacteria + dye].

3.5. In vitro cytotoxicity assays for the IONPs against human lung cancer cell line (A549)

The cytotoxic effects of IONPs on the human lung cancer cell line, A549 were investigated adopting MTT assay [33]. The IC_{50} value from the assay was estimated as 970 ± 5, µG/mL, in which concentration cell survival was reduced to nearly half compared to untreated cells. Further results of dose-dependent cytotoxicity of IONPs for 24-hour incubation confirmed that cytotoxic effect can be increased with increased dose over a given period of time (Figure 12).

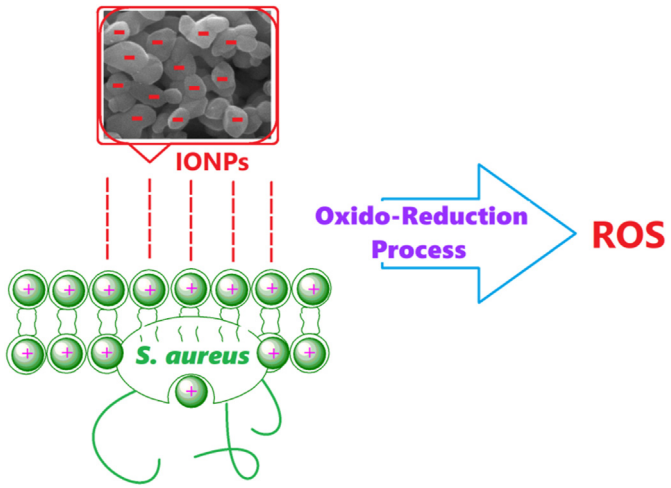

Scheme 2. Proposed model for bactericidal effect of IONPs against bacterial cells.

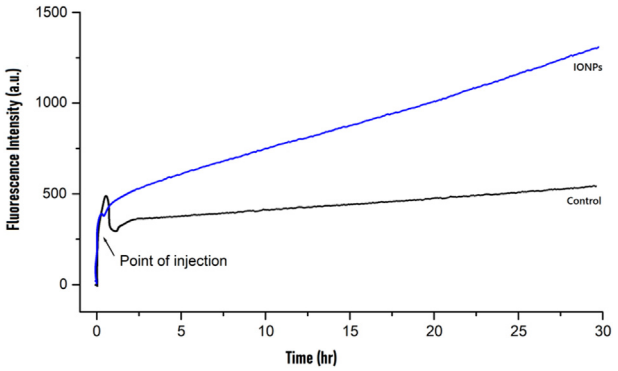

Figure 11. IONPs induced production of ROS and represent change in fluorescence intensity with DCFH-DA oxidation in presence of IONP for *S. aureus*.

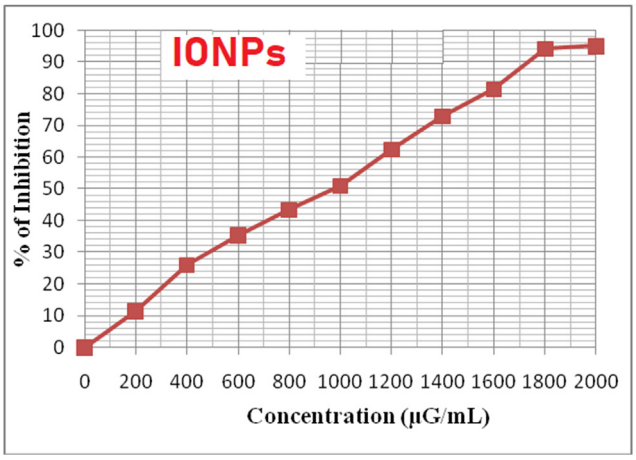

Figure 12. Dose dependent cytotoxic effect of IONPs on A549 cell lines in 24h incubation.

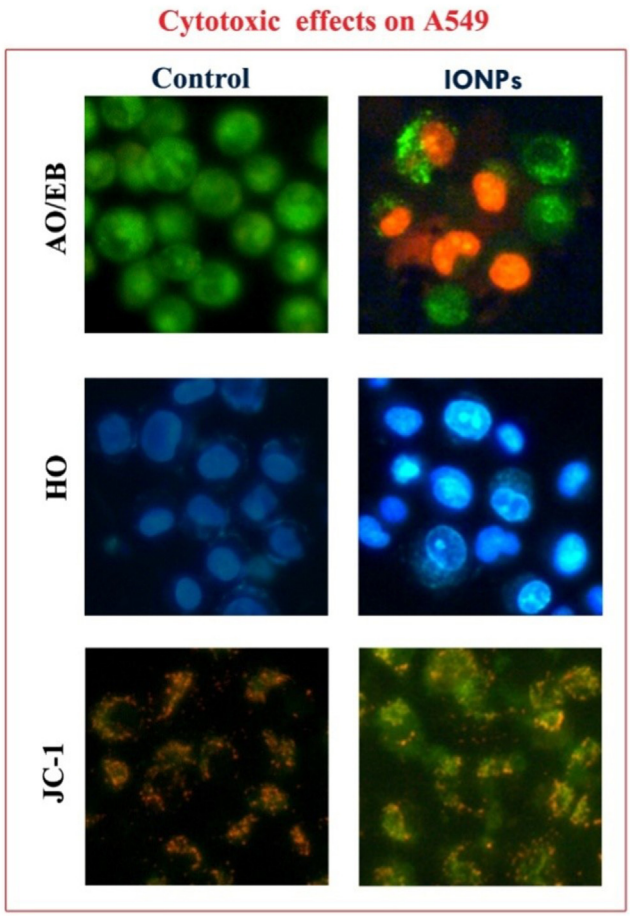

Figure 13. The result shows the cytotoxic effects of IONPs on A549 cancerous cell line through AO/EB, hoechst and JC1 staining. The image illustrates the staining of control and IONPs treated cells.

3.6. Morphological observation of apoptosis

Morphological changes are essential features of cells that undergo apoptotic cell death. The fluorescent based AO/EB and hoechst staining were used to illustrate the morphological changes induced by IONPs. Based on the morphological features, the cells in AO/EB staining were differentiated into normal/viable, apoptotic and necrotic. The normal cells have always been green fluoresced and also have uniform chromatin with intact cell membrane. Whereas apoptotic cells have various morphological characteristics, such as cell shrinkage, chromatin condensation, blebbing, and nuclear fragmentation, it has been fluoresced orange-red in color. Although the necrotic cells have fluoresced as orange-red, they will have the morphology that has swelled. AO/EB staining results suggest that incubating the IONPs for 24 h induces apoptosis in A549 cells than the necrosis mode of cell death (Figure 13). Compared with treated, the untreated cells have more viable cells. The results obtained from the hoechst stain are in good agreement with the AO/EB staining results. The IONPs treatments were found to induce morphological characteristics such as cell shrinkage, chromatin condensation, and fragmentation (Figure 13). Figure 14 demonstrates the percentage of apoptosis induced by IONPs observed through AO/EB and hoechst staining. It was demonstrated in AO/EB staining that IONPs treatment exhibit ~45% of cell death through apoptosis and ~6% by necrosis (Figure 14a) [34, 35, 36]. The % of cells exhibiting abnormalities was estimated as ~44% in hoechst study (Figure 14b). The findings showed that the majority of cells succumbed to cell death by apoptotic mode.

3.7. Loss of mitochondrial membrane potential (ΔΨm)

Mitochondria play a pivotal role in triggering the signalling of cell death via both intrinsic and extrinsic apoptosis pathway. In healthy cells, mitochondrial membrane potential has been preserved in such a way that mitochondria energize the cellular functions. Whereas in the case of apoptosis induced by a drug molecule, mitochondria begin to lose its membrane potential and releases cytochrome C into the cytosol. That further activates the caspases mediated apoptosis cell death and thus the anticancer agents were engineered to target cancer cell proliferation. In our study, using the cationic dye JC-1 was used to assess the collapse of ΔΨm induced by the IONPs. The JC-1 dye typically accumulates in mitochondria of healthy cells and emits orange-red fluorescence whereas it fluoresces green in cytosol when the mitochondrial membrane is depolarised. Our research results show that JC-1 stained cells emit green color under fluorescent microscopic observation, as induced by IONPs. Red color emission was observed during staining of untreated cell (Figure 12).

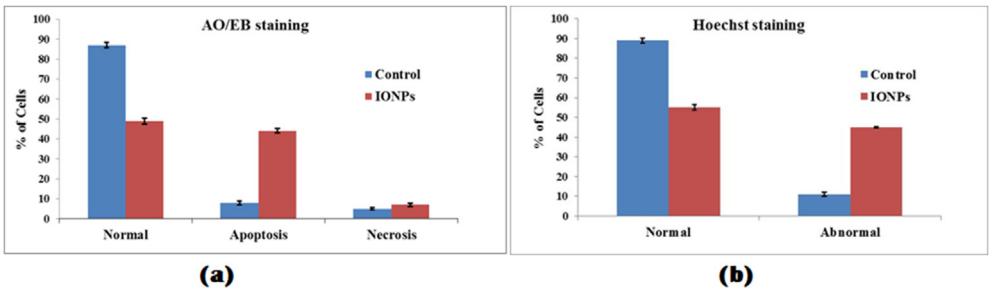

Figure 14. Cytotoxic effect of IONPs on A549 cells after exposure for 24 h through (a) AO/EB staining (b) Hoechst staining. Error bars represent mean ± SD (n = 3).

4. Conclusions

Herein, we describe the synthesis and morphological analysis of an iron oxide nanoparticle derived from thermal decomposition of a diiron(III)-Schiff base precursor. The morphology of the iron oxide nanoparticle (IONPs) has been analysed by powder XRD including scanning and transmission electron microscopy images. The average size of the hexagonal shaped cross linked porous nanoparticles was determined as ~97 nm and the hydrodynamic diameter was estimated 104 nm by dynamic light scattering studies. Study of the cytotoxic activity of IONPs on human lung cancer cell line (A549) reveals that nanoparticles induce the mode of apoptosis for the destruction of lung cancerous cells. The loss of mitochondrial membrane potential in lung cancer cell was further observed through depolarization pattern. Evaluation of antibacterial activity of the IONPs against different bacteria suggests that development of oxidative stress through opposite charged electromagnetic interactions and production of ROS remain the driving force for the potential antibacterial property. Thereby, IONPs hold a good promise to become a suitable alternate for clinically approved antibacterial agent. Further detailed investigations on drug delivery towards A549 cell lines as well as other cancerous cell lines may provide valuable information about therapeutic dose and side-effects in chemotherapy.

Declarations

Author contribution statement

Subrata Das: Conceived and designed the experiments; Performed the experiments; Analyzed and interpreted the data.

Sangharaj Diyali, G. Vinothini: Performed the experiments; Analyzed and interpreted the data.

Balaji Perumalsamy, Gowdhami Balakrishnan: Conceived and designed the experiments; Performed the experiments.

Thirumurugan Ramasamy: Performed the experiments; Analyzed and interpreted the data; Wrote the paper.

Dhanasekaran Dharumadurai: Analyzed and interpreted the data; Contributed reagents, materials, analysis tools or data; Wrote the paper.

Bhaskar Biswas: Conceived and designed the experiments; Analyzed and interpreted the data; Contributed reagents, materials, analysis tools or data; Wrote the paper.

Funding statement

Bhaskar Biswas was supported by Science and Engineering Research Board (SERB), India under Young Scientist Scheme (FT/CS-088/2013 dated 21/05/2014).

Competing interest statement

The authors declare no conflict of interest.

Additional information

No additional information is available for this paper.

References

[1] M.-D. Qian, Y.-L. Sun, Z.-Y. Hu, X.-F. Fang, J.-L. Zhu, X. Fan, Q. Liao, C.-F. Wu, H.-B. Sun, Fluorescent chemo-sensors based on "dually smart" optical micro/nano-waveguides lithographically fabricated with AIE composite resins, Mater. Horiz. (2020).

[2] A. Jain, S.K. Singh, S.K. Arya, S.C. Kundu, S. Kapoor, Protein nanoparticles: promising platforms for drug delivery applications, ACS Biomater. Sci. Eng. 4 (12) (2018) 3939–3961.

[3] (a) N. Fan, H. Liu, Q. Zhou, H. Zhuang, Y. Li, H. Li, Q. Xu, N. Li, J. Lu, Memory devices based on functionalized copolymers exhibiting a linear dependence of switch threshold voltage with the pendant nitro-azobenzene moiety content change, J. Mater. Chem. 22 (37) (2012) 19957–19963;
(b) D. Dey, S. Das, M. Patra, N. Kole, B. Biswas, Synthesis and characterization of a flower-structured ferromagnetic nickel oxide nanoparticle: investigation of photocatalytic activity, J. Org. Inorg. Chem. 1 (1) (2015) 1–8.

[4] C. Sanchez, P. Belleville, M. Popall, L. Nicole, Hybrid materials themed issue cluster-based inorganic–organic hybrid materials, Chem. Soc. Rev. 40 (2) (2011) 453–1152.

[5] C.-M. Chang, C.-H. Hsu, Y.-W. Liu, T.-C. Chien, C.-H. Sung, P.-H. Yeh, Interface engineering: broadband light and low temperature gas detection abilities using a nano-heterojunction device, Nanoscale 7 (47) (2015) 20126–20131.

[6] G. Hou, H. Zhang, G. Xie, K. Xiao, L. Wen, S. Li, Y. Tian, L. Jiang, Ultratrace detection of glucose with enzyme-functionalized single nanochannels, J. Mater. Chem. 2 (45) (2014) 19131–19135.

[7] S. Tong, C.A. Quinto, L. Zhang, P. Mohindra, G. Bao, Size-dependent heating of magnetic iron oxide nanoparticles, ACS Nano 11 (7) (2017) 6808–6816.

[8] W. Wu, C.Z. Jiang, V.A.L. Roy, Designed synthesis and surface engineering strategies of magnetic iron oxide nanoparticles for biomedical applications, Nanoscale 8 (47) (2016) 19421–19474.

[9] M.-H. Sun, S.-Z. Huang, L.-H. Chen, Y. Li, X.-Y. Yang, Z.-Y. Yuan, B.-L. Su, Applications of hierarchically structured porous materials from energy storage and conversion, catalysis, photocatalysis, adsorption, separation, and sensing to biomedicine, Chem. Soc. Rev. 45 (12) (2016) 3479–3563.

[10] P.C. Naha, Y. Liu, G. Hwang, Y. Huang, S. Gubara, V. Jonnakuti, A. Simon-Soro, D. Kim, L. Gao, H. Koo, D.P. Cormode, Dextran-coated iron oxide nanoparticles as biomimetic catalysts for localized and PH-activated biofilm disruption, ACS Nano 13 (5) (2019) 4960–4971.

[11] (a) Z. Chen, J.-J. Yin, Y.-T. Zhou, Y. Zhang, L. Song, M. Song, S. Hu, N. Gu, Dual enzyme-like activities of iron oxide nanoparticles and their implication for diminishing cytotoxicity, ACS Nano 6 (5) (2012) 4001–4012;
(b) S. Laurent, D. Forge, M. Port, A. Roch, C. Robic, L. V Elst, R.N. Muller, Magnetic iron oxide nanoparticles: synthesis, stabilization, vectorization, physicochemical characterizations and biological applications, Chem. Rev. 108 (6) (2008) 2064–2110.

[12] (a) L. Lartigue, C. Wilhelm, J. Servais, C. Factor, A. Dencausse, J.-C. Bacri, N. Luciani, F. Gazeau, Nanomagnetic sensing of blood plasma protein interactions with IONP macrophage uptake, ACS Nano 6 (3) (2012) 2665–2678;
(b) N.V. Long, T. Teranishi, Y. Yang, C.M. Thi, Y. Cao, M. Nogami, Iron oxide nanoparticles for next generation gas sensors, Int. J. Metall. Mater. Eng. 1 (119) (2015), 2372–2455.

[13] D. Kim, N. Lee, Y. Park, T. Hyeon, Recent development of nanoparticles for molecular imaging, Philos. Trans. R. Soc. A Math. Phys. Eng. Sci. 375 (2107) (2017).

[14] (a) S. Yu, V.M.H. Ng, F. Wang, Z. Xiao, C. Li, L.B. Kong, W. Que, K. Zhou, Synthesis and application of iron-based nanomaterials as anodes of lithium-ion batteries and supercapacitors, J. Mater. Chem. 6 (20) (2018) 9332–9367;
(b) B. Koo, H. Xiong, M.D. Slater, V.B. Prakapenka, M. Balasubramanian, P. Podsiadlo, C.S. Johnson, T. Rajh, E.V. Shevchenko, Hollow iron oxide nanoparticles for application in lithium ion batteries, Nano Lett. 12 (5) (2012) 2429–2435.

[15] Q. Ma, N. Izu, Y. Masuda, Ceria Polymer Hybrid Nanoparticles and Assembled Films for Coating Applications, ACS Appl. Nano Mater. 1 (5) (2018) 2112–2119.

[16] (a) X. Xia, Y. Zhang, D. Chao, C. Guan, Y. Zhang, L. Li, X. Ge, I.M. Bacho, J. Tu, H.J. Fan, Solution synthesis of metal oxides for electrochemical energy storage applications, Nanoscale 6 (10) (2014) 5008–5048;
(b) L. Li, X. Wang, Z. Ma, L. Liu, H. Wang, W. Zhang, X. Li, Electrospinning synthesis and electrocatalytic performance of iron oxide/carbon nanofibers composites as a low-cost efficient Pt-free counter electrode for dye-sensitized solar cells, Appl. Surf. Sci. 475 (2019) 109–116.

[17] N.V.S. Vallabani, S. Singh, Recent advances and future prospects of iron oxide nanoparticles in biomedicine and diagnostics, 3 Biotech 8 (6) (2018) 1–23.

[18] X. Ren, Y. Chen, H. Peng, X. Fang, X. Zhang, Q. Chen, X. Wang, W. Yang, X. Sha, Blocking autophagic flux enhances iron oxide nanoparticle photothermal therapeutic efficiency in cancer treatment, ACS Appl. Mater. Interfaces 10 (33) (2018) 27701–27711.

[19] Z. Shen, A. Wu, X. Chen, Iron oxide nanoparticle based contrast agents for magnetic resonance imaging, Mol. Pharm. 14 (5) (2017) 1352–1364.

[20] F. Li, Z. Liang, J. Liu, J. Sun, X. Hu, M. Zhao, J. Liu, R. Bai, D. Kim, X. Sun, T. Hyeon, D. Ling, Dynamically reversible iron oxide nanoparticle assemblies for targeted amplification of T1-weighted magnetic resonance imaging of tumors, Nano Lett. 19 (7) (2019) 4213–4220.

[21] L.M. Armijo, S.J. Wawrzyniec, M. Kopciuch, Y.I. Brandt, A.C. Rivera, N.J. Withers, N.C. Cook, D.L. Huber, T.C. Monson, H.D.C. Smyth, M. Osiński, Antibacterial activity of iron oxide, iron nitride, and tobramycin conjugated nanoparticles against pseudomonas aeruginosa biofilms, J. Nanobiotechnol. 18 (1) (2020) 1–27.

[22] N. Zare, A. Zabardasti, A. Mohammadi, F. Azarbani, Synthesis of spherical Fe_3O_4 nanoparticles from the thermal decomposition of iron (III) nano-structure complex: DFT studies and evaluation of the biological activity, Bioorg. Chem. 80 (April) (2018) 334–346.

[23] L. Zhang, H. Xie, Y. Liu, J. Wang, Research on nanotoxicity of an iron oxide nanoparticles and potential application, Toxicol. Open Access 03 (03) (2017) 1–7.

[24] B. Biswas, M. Mitra, J. Adhikary, G.R. Krishna, P.P. Bag, C.M. Reddy, N. Aliaga-Alcalde, T. Chattopadhyay, D. Das, R. Ghosh, Synthesis, X-ray structural and magnetic characterizations, and epoxidation activity of a new bis(μ-acetato)(μ-alkoxo)dinuclear iron(III) complex, Polyhedron 53 (2013) 264–268.

[25] D. Dey, G. Kaur, M. Patra, A.R. Choudhury, N. Kole, B. Biswas, A perfectly linear trinuclear zinc-schiff base complex: synthesis, luminescence property and photocatalytic activity of zinc oxide nanoparticle, Inorg. Chim. Acta. 421 (2014) 335–341.

[26] S. Das, A. Sahu, M. Joshi, S. Paul, M. Shit, A.R. Choudhury, B. Biswas, Ligand-centered radical activity by a zinc-schiff-base complex towards catechol oxidation, ChemistrySelect 3 (38) (2018) 10774–10781.

[27] C.K. Pal, S. Mahato, M. Joshi, S. Paul, A.R. Choudhury, B. Biswas, Transesterification activity by a zinc(II)-schiff base complex with theoretical interpretation, Inorg. Chim. Acta. 506 (February) (2020) 119541.

[28] M. Karar, S. Paul, B. Biswas, T. Majumdar, A. Mallick, A newly developed highly selective Zn_2+-AcO- ion-pair sensor through partner preference: equal efficiency under solitary and colonial situation, Dalton Trans. 47 (20) (2018) 7059–7069.

[29] M. Balouiri, M. Sadiki, S. Koraichi Ibnsouda, Methods for in vitro evaluating antimicrobial activity: a review, J. Pharm. Anal. 6 (2) (2016) 71–79.

[30] A. Norazah, C.H. Teh, W.A. Nazni, W.A. Nurulhusna, H.L. Lee, Determination of antibacterial activity and minimum inhibitory concentration of larval extract of fly via resazurin-based turbidometric assay, BMC Microbiol 17 (1) (2017) 1–8.

[31] H. Possel, H. Noack, W. Augustin, G. Keilhoff, G. Wolf, 2,7-dihydrodichlorofluorescein diacetate as a fluorescent marker for peroxynitrite formation, FEBS Lett. 416 (2) (1997) 175–178.

[32] D. Díaz-García, P.R. Ardiles, S. Prashar, A. Rodríguez-Diéguez, P.L. Páez, S. Gómez-Ruiz, Preparation and study of the antibacterial applications and oxidative stress induction of copper maleamate-functionalized mesoporous silica nanoparticles, Pharmaceutics 11 (1) (2019) 1–18.

[33] T. Mosmann, Rapid colorimetric assay for cellular growth and survival: application to proliferation and cytotoxicity assays, J. Immunol. Methods 65 (1–2) (1983) 55–63.

[34] D.L. Spector, R.D. Goldman, L.A. Leinwand, Culture and Biochemical Analysis of Cells: A Laboratory Manual, 1998.

[35] G.P.A.H. Kasibhatla, D. Finucane, T. Brunner, E.B. Wetzel, D.R. Green, Protocol: staining of suspension cells with Hoechst 33258 to detect apoptosis cell, in: C. Press (Ed.), A Laboratory Manual Culture and Biochemical Analysis of Cells: USA, 1998.

[36] M. Reers, T.W. Smith, L.B. Chen, Aggregate formation of a carbocyanine as a quantitative fluorescent indicator of membrane potential, Biochem 30 (18) (1991) 4480–4486.

[37] A. Bishnoi, S. Kumar, N. Joshi, Wide-Angle X-Ray Diffraction (WXRD), Elsevier Inc., 2017.

[38] N. Tran, A. Mir, D. Mallik, A. Sinha, S. Nayar, T.J. Webster, Bactericidal effect of iron oxide nanoparticles on *Staphylococcus aureus*, Int. J. Nanomed. 5 (1) (2010) 277–283.

[39] S.V. Gopal, R. Mini, V.B. Jothy, I.H. Joe, Synthesis and characterization of iron oxide nanoparticles using DMSO as a stabilizer, Mater. Today Proc. 2 (3) (2015) 1051–1055.

[40] S. Das, M. Garai, M. Patra, A. Mallick, M. Maji, B. Biswas, Recyclable ferromagnetic iron oxide nanocatalyst for the degradation of methylene blue, J. Inst. Chem. 88 (September) (2016) 50–64.

[41] G.K. Auer, D.B. Weibel, Biochem 56 (29) (2017) 3710–3724.

[42] M. Arakha, S. Pal, D. Samantarrai, T.K. Panigrahi, B.C. Mallick, K. Pramanik, B. Mallick, S. Jha, Antimicrobial activity of iron oxide nanoparticle upon modulation of nanoparticle-bacteria interface, Sci. Rep. 5 (2015) 1–12.

[43] S.A. Mahdy, Q.J. Raheed, P.T. Kalaichelvan, Antimicrobial activity of zero-valent iron nanoparticles, Int. J. Mod. Eng. Res. 2 (1) (2012) 578–581.

[44] M.E. McBee, Y.H. Chionh, M.L. Sharaf, P. Ho, M.W.L. Cai, P.C. Dedon, Production of superoxide in bacteria is stress- and cell state-dependent: a gating-optimized flow cytometry method that minimizes ROS measurement artifacts with fluorescent dyes, Front. Microbiol. 8 (MAR) (2017) 1–17. Art 459.

[45] D. Touati, Iron and oxidative stress in bacteria 1, Arch. Biochem. Biophys. 373 (1) (2000) 1–6.

[46] H.V. Acker, J. Gielis, M. Acke, F. Cools, P. Cos, T. Coenye, The role of reactive oxygen species in antibiotic-induced cell death in Burkholderia cepacia complex bacteria, PLoS One 11 (7) (2016) 1–20.

[47] I. Albesa, M.C. Becerra, P.C. Battán, P.L. Páez, Oxidative stress involved in the antibacterial action of different antibiotics, Biochem. Biophys. Res. Commun. 317 (2) (2004) 605–609.

[48] N. Durán, M. Durán, M.B. de Jesus, A.B. Seabra, W.J. Fávaro, G. Nakazato, Silver nanoparticles: a new view on mechanistic aspects on antimicrobial activity, Nanomedicine 12 (3) (2016) 789–799.

[49] C. Lee, J.Y. Kim, W.I. Lee, K.L. Nelson, J. Yoon, D. L, Bactericidal effect of zero-valent iron nanoparticles on *Escherichia coli*, Environ. Sci. Technol. 42 (13) (2008) 4927–4933.